





Article

Microwave-Assisted Synthesis of Flower-like MnMoO₄ Nanostructures and Their Photocatalytic Performance

Muthamizh Selvamani ¹, Arulvarman Kesavan ^{2,*}, Arunachalam Arulraj ³ , Praveen C. Ramamurthy ⁴, Mostafizur Rahaman ⁵, Saravanan Pandiaraj ⁶, Muthu Thiruvengadam ⁷ , Elisban Juani Sacari Sacari ⁸ , Elmer Marcial Limache Sandoval ^{9,*} and Mangalaraja Ramalinga Viswanathan ^{10,11} 

¹ Department of Physiology, Saveetha Dental College & Hospitals, Saveetha Institute of Medical & Technical Sciences, Saveetha University, Chennai 600077, Tamil Nadu, India; muthamizh23@gmail.com

² Department of Physics & Nanotechnology, SRM Institute of Science & Technology, Kattankulathur 603203, Tamil Nadu, India

³ Departamento de Electricidad, Facultad de Ingeniería, Universidad Tecnológica Metropolitana (UTEM), Macul, Santiago 7800002, Chile; arul@utem.cl

⁴ Department of Materials Engineering, Indian Institute of Science, Bangalore 560012, Karnataka, India; praveen@iisc.ac.in

⁵ Department of Chemistry, College of Science, King Saud University, P.O. Box 2455, Riyadh 11451, Saudi Arabia; mrahaman@ksu.edu.sa

⁶ Department of Self-Development Skills, King Saud University, P.O. Box 2455, Riyadh 11451, Saudi Arabia; psaravanan.c@ksu.edu.sa

⁷ Department of Applied Bioscience, College of Sanghuh Life Science, Konkuk University, Seoul 05029, Republic of Korea; thiruv30@gmail.com

⁸ Centro de Energías Renovables de Tacna, Facultad de Ciencias, Universidad Nacional Jorge Basadre Grohmann, Avenida Miraflores S/N, Ciudad Universitaria, Tacna 23003, Peru; esacaris@unjb.edu.pe

⁹ Grupo de Investigación HIDROCIENCIA, Facultad de Ciencias de la Salud, Universidad Privada de Tacna, Av. Jorge Basadre Grohmann S/N Pocollay, Tacna 23003, Peru

¹⁰ Faculty of Engineering and Sciences, Universidad Adolfo Ibáñez, Diagonal las Torres 2640, Peñalolén, Santiago 7941169, Chile; mangal@uai.cl

¹¹ Department of Mechanical Engineering, Faculty of Engineering, Karpagam Academy of Higher Education, Coimbatore 641021, Tamil Nadu, India

* Correspondence: arulkvarman@gmail.com (A.K.); elmlimache@upt.pe (E.M.L.S.)



Citation: Selvamani, M.; Kesavan, A.; Arulraj, A.; Ramamurthy, P.C.; Rahaman, M.; Pandiaraj, S.; Thiruvengadam, M.; Sacari Sacari, E.J.; Limache Sandoval, E.M.;

Viswanathan, M.R. Microwave-Assisted Synthesis of Flower-like MnMoO₄ Nanostructures and Their Photocatalytic Performance. *Materials* **2024**, *17*, 1451. <https://doi.org/10.3390/ma17071451>

Academic Editors: Vlassios Likodimos and Andrea Petrella

Received: 30 November 2023

Revised: 27 December 2023

Accepted: 2 February 2024

Published: 22 March 2024



Copyright: © 2024 by the authors. Licensee MDPI, Basel, Switzerland. This article is an open access article distributed under the terms and conditions of the Creative Commons Attribution (CC BY) license (<https://creativecommons.org/licenses/by/4.0/>).

Abstract: This article describes an affordable method for the synthesis of MnMoO₄ nanoflowers through the microwave synthesis approach. By manipulating the reaction parameters like solvent, pH, microwave power, and irradiation duration along this pathway, various nanostructures can be acquired. The synthesized nanoflowers were analyzed by using a powder X-ray diffractometer (XRD), field emission scanning electron microscopy (FE-SEM) with energy dispersive X-ray spectroscopy (EDS), Fourier transform infrared spectroscopy (FT-IR), and UV–vis diffuse reflectance spectroscopy (UV–DRS) to determine their crystalline nature, morphological and functional group, and optical properties, respectively. X-ray photoelectron spectroscopy (XPS) was performed for the examination of elemental composition and chemical states by qualitative and quantitative analysis. The results of the investigations demonstrated that the MnMoO₄ nanostructures with good crystallinity and distinct shape were formed successfully. The synthesized MnMoO₄ nanoflowers were tested for their efficiency as a photocatalyst in the degradation studies of methylene blue (MB) as model organic contaminants in an aqueous medium under visible light, which showed their photocatalytic activity with a degradation of 85%. Through the band position calculations using the electronegative value of MnMoO₄, the photocatalytic mechanism of the nanostructures was proposed. The results indicated that the effective charge separation, and transfer mechanisms, in addition to the flower-like shape, were responsible for the photocatalytic performance. The stability of the recovered photocatalyst was examined through its recyclability in the degradation of MB. Leveraging MnMoO₄'s photocatalytic properties, future studies may focus on scaling up these processes for practical and large-scale environmental remediation.

Keywords: MnMoO₄ flower; photocatalyst; visible light active; environmental

1. Introduction

Poisonous and dangerous substances affect the ecological integrity and ecosystems of the globe, necessitating comprehensive environmental organization and rehabilitation [1]. The persistence, non-biodegradability, and bioaccumulation of numerous biochemical pollutants endanger social wellbeing and reduce financial wellbeing, creating significant problems for environmental groups. The rapid industrial expansion, fueled by unsustainable technical breakthroughs, can result in industrial wastewater, which is generated in significant quantities worldwide each year, increasing chemical risks [2]. These substances have been strongly connected to significant consequences and long-term impacts, the majority of which are related to acute water poisoning. To address the quick identification and detection of these problematic substances, proper risk assessment methodologies are required [3]. The contamination of water is caused by a variety of pollutants, including inorganic (salts, caustic metal ions, and metal oxides) and organic (pesticides, fertilizers, phenol, and dyes) pollutants, agricultural runoff, and so on [4–6]. The methods for removing organic matter can be distinctly separated into three groups: (i) physical, (ii) chemical, and (iii) biological, which include precipitation [7], ion exchange [8], sonochemical degradation [9], adsorption [10], and various advanced oxidation process techniques such as Fenton [11], photo-Fenton [12], photocatalysis [13], etc.

The degradation of environmental contaminants using photocatalysis is an interesting approach. With its capacity to break down different pollutants and convert light energy into chemical energy, photocatalysis has captured the attention of researchers studying possible applications of today's technological advancements. This opens up promising avenues for the removal of potentially dangerous contaminants from the environment [14,15]. Photocatalysis is the succession of the oxidation and reduction processes caused by electrons and holes stimulated by photons. The photocatalytic performance of the catalysts will eventually be linked with its shape, chemical and surface characteristics, and crystallinity. Hence, using the photocatalysis approach as a strategy for water purification necessitates the active use of UV and visible light, as well as the usage of highly complicated photocatalysts. The development of a photocatalysis system that counteracts the visible and UV light is critical for removing organic pollutants from the wastewater [16,17].

Molybdenum (Mo)-based nanomaterials have been largely studied in the field of photocatalytic pollutant degradation. They have been extensively used as environmental remediation materials because of their exceptional performance in photocatalysis. Molybdenum oxides have garnered significant attention in recent times for their potential applications in several domains, such as humidity sensors, magnetic fields, the microwave approach, optical fibers, scintillator materials, photoluminescence devices, catalysis, and electrochemical sensors, owing to their physiochemical characteristics [18–21]. Adding certain precious metals to the oxides can enhance their optical, catalytic, and sensing properties. In recent decades, several metal molybdates with various shapes and characteristics have been documented [22]. Molybdates are compounds containing molybdenum oxy anions in which molybdenum has the formal oxidation number of +6. Molybdates are a significant group of transition metal oxides. They possess an extremely large bivalent cation with an ionic radius >0.99 for scheelite structures, such those of Ba, Sr, Pb, or Ca. In this way, the binary metal oxide manganese molybdate (MnMoO₄) has received a lot of research interest recently because of its affordability, viability as oxidation states, improved electrical conductivity, and good thermal and chemical stability, allowing it to achieve superior electrochemical performance [23,24].

Additionally, a wide range of rich redox reactions are offered by the metal ions in binary metal oxides. Among the binary metal oxides, MnMoO₄ has attracted a lot of attention due to its low cost, environmental friendliness, excellent electrical conductivity,

broad working voltage window, and remarkable stability. Furthermore, MnMoO_4 exhibits outstanding qualities including natural abundance, low toxicity, and a stable crystal structure. Its enormous theoretical specific capacitance and strong electrical conductivity make it environmentally beneficial. The binary metal naturally has a wide operating voltage window and a high retention capacity for energy storage devices [25].

In the present investigation, the microwave synthesis methodology was utilized for the production of MnMoO_4 . The morphology of synthesized MnMoO_4 was confirmed to be flower-like structures. The structural and optical properties of synthesized MnMoO_4 were confirmed and the phase validation was performed. The synthesized catalyst was utilized for the degradation of methylene blue (MB) through the photocatalytic degradation process as a representative organic toxin.

2. Materials and Methods

The basic starting materials used in the synthesis of MnMoO_4 such as manganese acetate $\text{Mn}(\text{CH}_3\text{CO}_2)_2 \cdot (\text{H}_2\text{O})$, ammonium molybdate $(\text{NH}_4)_6\text{Mo}_7\text{O}_{24}$, and methylene blue (MB) were analytical grade chemicals acquired from SRL, India. Two solvents were utilized in the synthesis process: ethanol and double-distilled water (DDW).

2.1. Synthesis of MnMoO_4 Flowers

The simple microwave approach was used for producing MnMoO_4 flowers. The typical methodology involved dissolving 2 mmol of $\text{Mn}(\text{CH}_3\text{CO}_2)_2 \cdot (\text{H}_2\text{O})$ in 30 mL of polyethylene glycol and 0.27 mmol of ammonium molybdate in 30 mL of polyethylene glycol separately at 70 °C, with each solution named as solution A and solution B. Both the solutions were added to each other drop by drop. The pH of the reaction medium was brought to 11 through introducing ethylenediamine; the suspension was subjected to microwave radiation at 750 W for 7 min. The final sample was cleaned multiple times with DDW and ethanol before being oven-dried for 6 h at 90 °C. The resultant powder was ultimately calcined for 2 h at 500 °C to obtain the crystalline MnMoO_4 nanoflowers.

2.2. MnMoO_4 Nanoflower Investigated with Different Characterizations

The XRD method was used to determine the sample's crystallinity, and a Rich Siefert 3000 diffractometer was used to measure the sample's response to $\text{Cu-K}_{\alpha 1}$ radiation ($\lambda = 1.5406$). X-ray photoelectron spectroscopy (XPS) performed by Omicron nanotechnology-ESCA-14, Germany, was employed to define the chemical structure of the manganese molybdate. The FT-IR spectroscopic analysis (using a Perkin-Elmer spectrophotometer) was used to examine the compound's functional group. For the sample analysis, the KBr pellet technique was employed. The Raman-11 Nano Photon Corporation Instrument, manufactured in Japan, was utilized for the Raman analysis. Using a Perkin-Elmer spectrophotometer, the material's optical properties were evaluated. By using field emission scanning electron microscopy (FE-SEM), HITACHI SU6600, FEI, Hitachi High-Technologies, Tokyo, Japan, the morphology of manganese molybdate was recorded.

3. Results

3.1. Structural Analysis by XRD

Figure 1 displays the synthesized MnMoO_4 XRD pattern. A diffraction peak was allocated to the space group $p2/c$ of JCPDS Card No. 01-082-2166, which corresponds to the monoclinic structure of MnMoO_4 . It displays the peaks corresponding to (110), (-111), (111), (021), (201), (220), (002), (-221), (-202), (310), (130), (022), (-222), (311), (400), (-313), (-223), (-403), (402), (150), (-151), (133), (-621), (060), and (531) of monoclinic MnMoO_4 . The lattice specifications of MnMoO_4 are $a = 10.49 \text{ \AA}$, $b = 9.52 \text{ \AA}$, $c = 7.15 \text{ \AA}$, and $\beta = 106.33^\circ$. The synthesized material is highly crystalline in nature, as seen through the strong diffraction of MnMoO_4 . Furthermore, there were no further impurity peaks found [26].

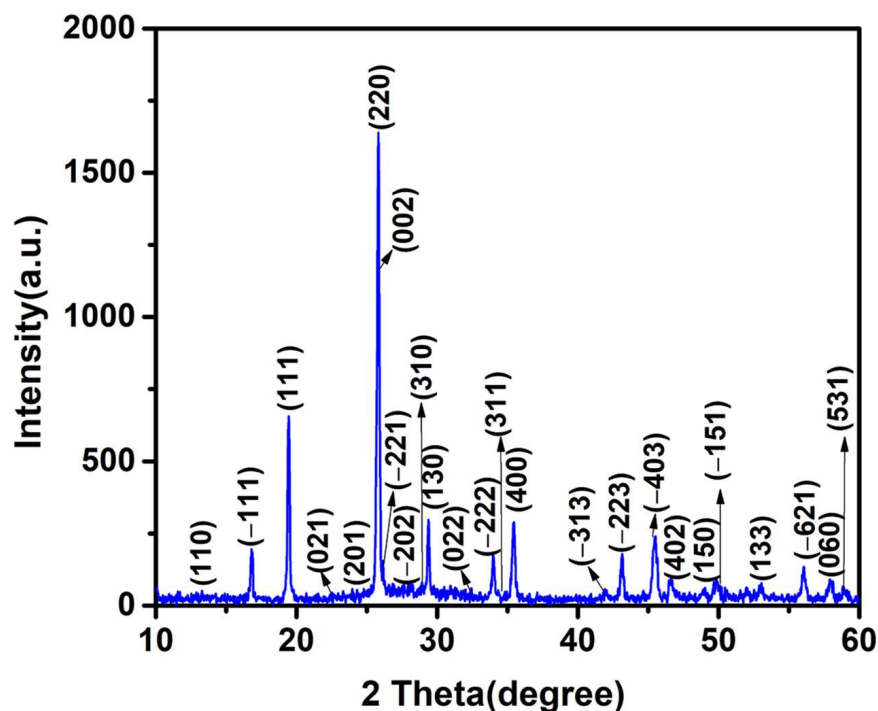


Figure 1. XRD spectrum of synthesized MnMoO₄ flowers.

3.2. XPS Investigation

The MnMoO₄ nanostructures were subjected to XPS examination in order to verify the elements' oxidation states, binding energies, and chemical composition. The survey XPS spectrum of MnMoO₄ is displayed in Figure 2a. It displays the occurrence of Mn, Mo, and O in the produced MnMoO₄. This outcome aligns with the EDAX study. Additionally, the following section discusses the high-resolution XPS spectra of the produced MnMoO₄ nanoflowers for Mn 2p, Mo 3d, and O 1s. The XPS spectrum of Mn 2p is shown in Figure 2b. Doublet peaks are seen at 641.5 and 653.7 eV, respectively, which correspond to Mn 2p_{3/2} and Mn 2p_{1/2}. This indicates that the oxidation state of +2 of the Mn in the sample is present. The Mo 3d XPS spectrum is seen in Figure 2c, with two peaks at 228.4 and 231.5 eV, respectively, that belong to Mo 3d. The measured Mo 3d_{3/2} and Mo 3d_{5/2} doublets' separation was found to be 3.1 eV, corresponding to the Mo +6 oxidation state [27,28]. The O 1s peak has a prominent component centered at 529.2 eV with a low binding energy; this is indicative of the oxide that forms O²⁻ with components of manganese and molybdenum (Mn–O–Mo), and 531.9 eV corresponds to the surface hydroxyl group, as shown in Figure 2d [29]. The C1s peak is fitted with two peaks at 285.6 and 289.3 eV which belong to C 1s and C–O, respectively [30]. Further, by referring to the previous literature, quantification of the synthesized catalyst MnMoO₄ is calculated. Mn, Mo, and O elements are displayed along with an error bar in atomic % from the high-resolution XPS spectra; the relevant values are provided in Table 1 [31].

Table 1. Atomic % of the elements present in MnMoO₄.

Elements	Mn	Mo	O
Atomic %	19.54	44.42	36.04

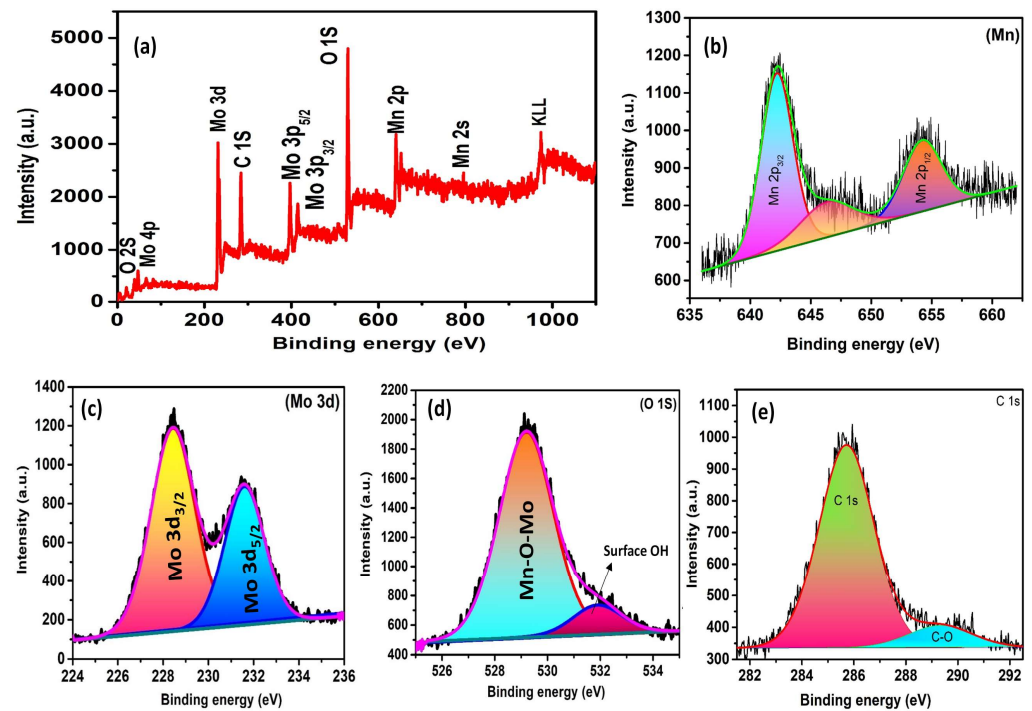


Figure 2. The XPS (a) survey spectrum of MnMoO₄; (b–e) core-level spectrum of Mn, Mo, O, and C, respectively.

3.3. Structural and Optical Properties

Figure 3a displays the synthesized MnMoO₄ Raman spectrum. The measured bands for the synthesized MnMoO₄ correspond to the different modes. MnMoO₄ was found to have bands at 902, 782, 542, 402, 338, and 273 cm⁻¹. The Raman peaks at 902 and 782 cm⁻¹ are caused by symmetrical stretching of Mo-O-Mo and asymmetrical stretching of ν as Mo=O [32]. The Mo-O-Mo bond, which is due to mutual oxygen atoms of 2 and 3 octahedral MoO₆, due to symmetric and asymmetric stretching, is confirmed by peaks at 542 and 402 cm⁻¹ [33]. The signal that was seen at 273 cm⁻¹ is consistent with the double bond O=Mo=O in MnMoO₄ nanostructures due to wagging. Figure 3b shows the FT-IR spectra of the synthesized MnMoO₄. The surface hydroxyl O-H bond vibration is shown by a wide band seen at 3436 cm⁻¹. The H-O-H distortion mode of the surface hydroxyl assembly is represented by the band at 1637 cm⁻¹ [34]. Peaks of MnMoO₄ are seen at around 864 and 910 cm⁻¹, which corresponded to the stretching and bending vibration of Mo=O and Mo-O-Mo, respectively. The optical property of produced MnMoO₄ was examined using UV-vis diffuse reflectance spectroscopy (DRS) and the obtained result is presented in Figure 2c. The robust absorption peak at 303 nm is due to the switch among bands of O 2p and Mn 3d levels in the MnMoO₄ [35]. The bandgap (E_g) of the manufactured MnMoO₄ was calculated through Tauc's plot (Equation (1)).

$$(h\nu\alpha)^{1/n} = A(h\nu - E_g) \quad (1)$$

The synthesized MnMoO₄ presented a direct bandgap of 2.59 eV, which is shown in Figure 3c,d [36]. Additionally, the conduction band (CB) and valence band (VB) positions were identified by using Equations (2) and (3):

$$E_{VB} = X - E^e + 0.5E_g \quad (2)$$

$$E_{CB} = E_{VB} - E_g \quad (3)$$

The conduction band (CB) edge potential is denoted by E_{CB} , the bandgap energy is represented by E_g , the valence band (VB) edge potential is represented by E_{VB} , and the electronegativity of $MnMoO_4$ is represented by X (5.94 eV). The E_{CB} value for the $MnMoO_4$ flowers is determined to be -0.305 eV using these calculations. Furthermore, the E_{VB} value is estimated as 1.26 eV. The oxygen vacancies' role in the valence band edge increasing and the conduction band edge reducing is verified by these computations. To enable effective photocatalytic activity, the oxygen vacancies ideally stimulate the creation of sub-bands (below but near to CB) that both limit electron-hole recombination and function as amplifiers for the shift of electrons.

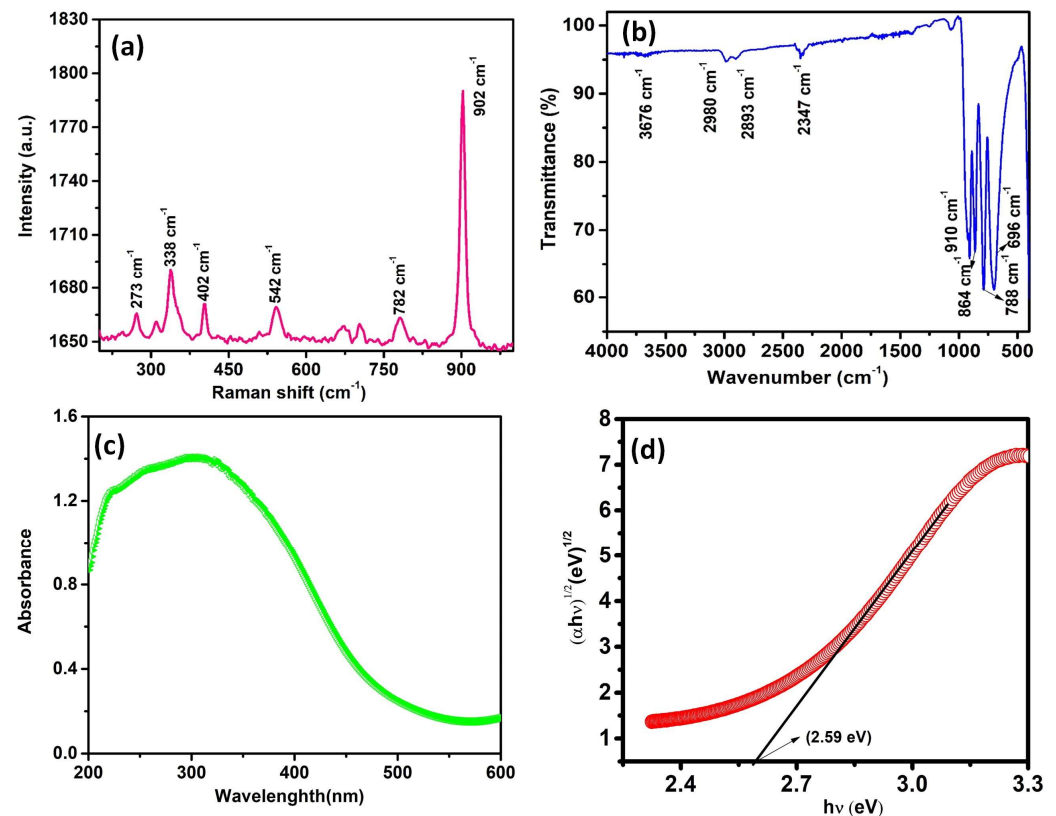


Figure 3. (a–d) The Raman, FT-IR, and DRS-UV spectra corresponding to the bandgap of the prepared $MnMoO_4$ flowers.

4. Morphological Analysis

The FE-SEM images of $MnMoO_4$ revealed the formation of flower-like structures, as shown in Figure 4a–d. These nanoflowers exhibited a high degree of $MnMoO_4$ nanopetal arrangement to form a uniform flower-like morphology with size of $1 \mu m$. The $MnMoO_4$ nanoflowers are assembled from discrete nanopetals with a thickness of a nanometer [37]. This hierarchical flower has more dense petals which may favor the photocatalytic activity due to the involvement of a greater number of nanopetals at a time. The EDS analysis (Figure 4d) confirmed the elemental composition of the $MnMoO_4$ flowers. The spectrum displayed peaks corresponding to manganese (Mn), molybdenum (Mo), and oxygen (O), respectively.

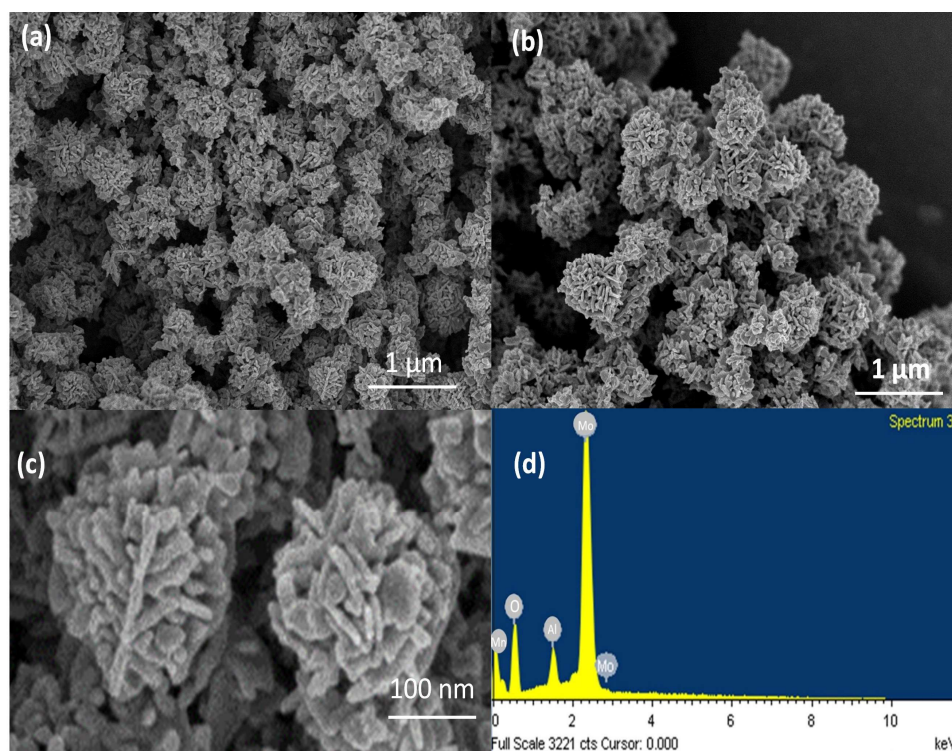


Figure 4. (a–c) The FE-SEM images of MnMoO₄ and (d) the corresponding EDS.

5. Photodegradation of MB in the Presence of MnMoO₄

Figure 5A portrays the photocatalytic action of the manufactured MnMoO₄ flowers studied regarding the breakdown of methylene blue (MB) dye in the presence of visible light irradiation. Two types of control experiments were conducted by taking a blank dye (MB) solution of 1×10^{-5} and a dye with MnMoO₄ in dark conditions to compare the photocatalytic action of the material in the existence of light. The typical procedure of combining dye with a catalyst in the presence of light involves the addition of 100 mL of a 1×10^{-5} M MB dye solution to a 250 mL beaker along with 50 mg of the catalyst (MnMoO₄). The mixture of pollutant and catalyst was obtained in the dark, preventing contact with light, to achieve the adsorption–desorption balance of the photocatalyst and dye [38,39]. Among the above two reaction mixtures, the pure dye solution and the dye with the catalyst were maintained in the dark, the dye was set with light, and the material with dye was exposed to the visible light after half an hour while being constantly stirred with magnetic stirrer. At regular intervals of every 10 min, all of the three sets of reaction mixture were collected by using a syringe filter to avoid sample contamination during UV-vis analysis. Figure 5B shows the C/C_0 vs time plot of methylene blue in the dark, methylene blue in light, and methylene blue in the dark and light exposure condition in the presence of the photocatalyst. The color of the MB solution changes from dark blue to leucomethylene blue (colorless) as the MB decrease happens, which demonstrates the photodegradation plot of the pollutant molecules proposed by observing the decrease in the pollutant content under solar light. Firstly, the degradation of the MB solution was estimated in the absence of light to observe the chemical progression in the absence of light. Upon illumination, the pollutant concentration was gradually removed through photoreaction; the concentration in the dye deprived of any catalyst was noted to be 2.9% at 50 min, and the dye with the catalyst in the dark condition displayed the adsorption of the pollutant on the outer layer of catalyst, with the concentration being 13% at 50 min [40]. As the photocatalyst reaction proceeds with the MnMoO₄ flowers as the photocatalyst, it was seen that the absorption maximum of the dye peaks at 665 nm, reducing gradually at 50 min, with 85% of the dye observed, as shown in Figure 6a. The photocatalytic property

of the present catalyst is matched with that previously stated in the literature and currently proposed in Table 2.

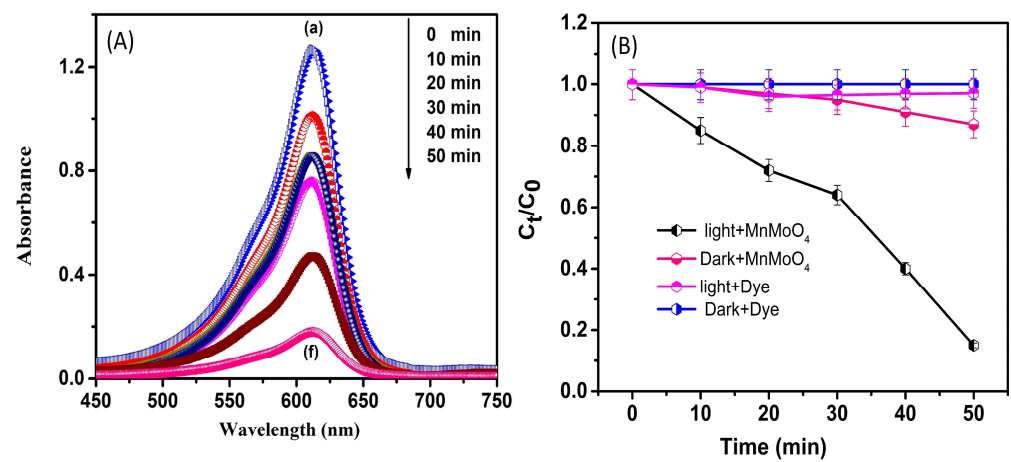


Figure 5. (A) The absorption spectra of methylene blue degradation with MnMoO₄ flowers from 0 to 50 min (represented by (a) to (f)) during photocatalysis, and (B) C_t/C_0 vs. time plot of methylene blue.

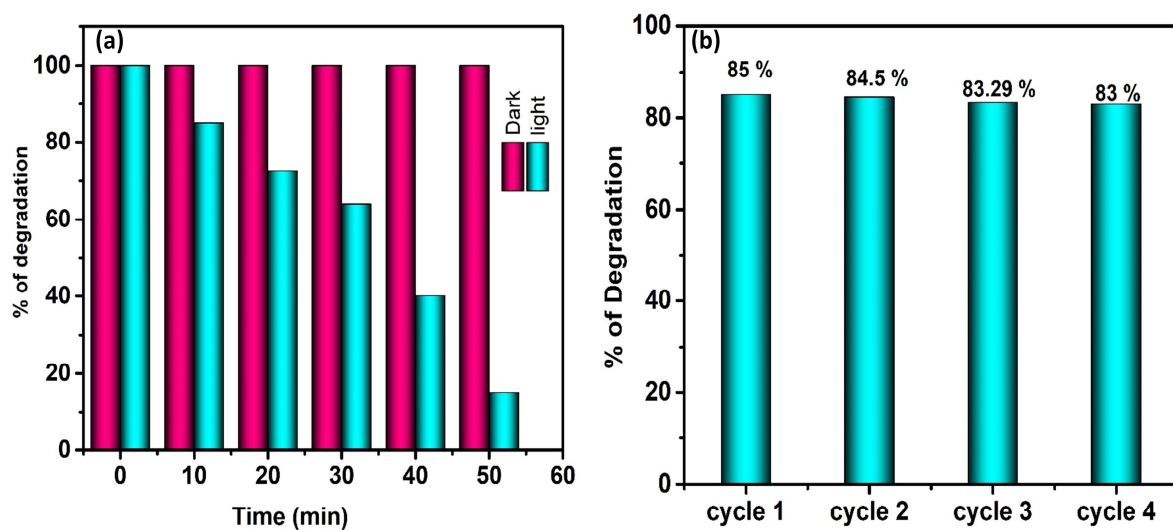


Figure 6. (a) The degradation efficacy % with respect to time; (b) the cycling test of the photocatalytic degradation of pollutants on MnMoO₄ flowers.

Table 2. Comparison with other photocatalysts for the degradation of MB.

Catalyst	Dye	Amount of Catalysts	Degradation Efficiency	Degradation Time	Reference
ZnO/g-C ₃ N ₄	MB	100 mg	98%	180 min	[41]
N-doped carbon/CuO-Fe ₂ O ₃	MB	100 mg	97.4%	180 min	[42]
N-doped ZnO	MB	100 mg	93.2%	30 min	[43]
Cerium-doped copper aluminate	MB	25 mg	72.49%	90 min	[44]
Cu ₂ O/BiVO ₄	MB	50 mg	72.9%	160 min	[45]
MnMoO ₄	MB	50 mg	85%	50 min	Present study

Cycling Test to Remove Pollutants Using Photocatalysis

The photodegradation and stability of MnMoO₄ flowers toward MB dye was examined under identical reaction conditions. The MnMoO₄ photocatalyst was separated after the degrading process and given a thorough deionized water and ethanol wash. Before using

the recovered catalyst in a second run, it was desiccated at 100 °C in a hot-air oven. The MB dye deterioration during the four runs is displayed in Figure 6b. In the consecutive four cycles with MnMoO₄ flowers, the MB dye degradation percentages were 85.00, 84.50, 83.29, and 83.00, respectively, with a 50 min reaction runtime. The MnMoO₄ flowers deterioration efficiency was not altered significantly, even after the consecutive four tests. Stability and reusability are essential components for a photocatalyst to be used in practical applications. The structural consistency of the MnMoO₄ flowers was tested later through X-ray diffraction analysis and morphological studies after four cycles; the obtained results are presented in Figure 7a,b. These results demonstrate that except from a decline in peak strength, morphology, and repeatable action, there are no observable structural changes during the photocatalytic processes. Consequently, it is possible to utilize wastewater management schemes for a long time.

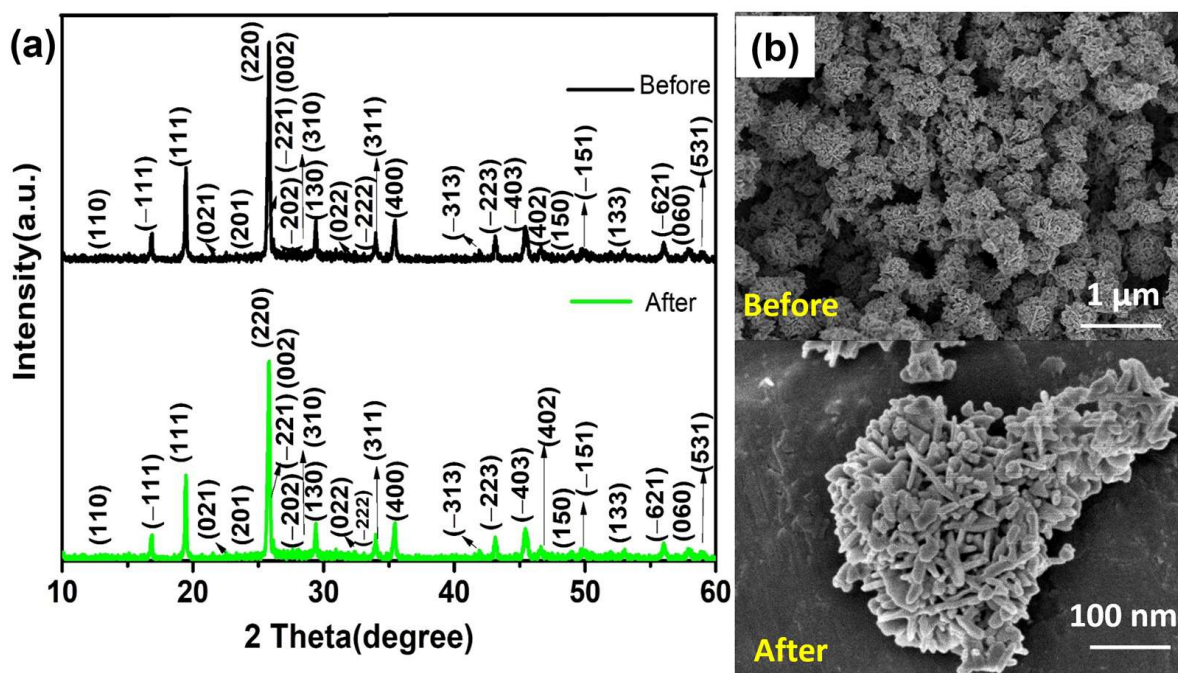


Figure 7. (a) The XRD patterns and (b) the FE-SEM analysis of MnMoO₄ flowers synthesized and after catalytic reaction.

6. Conclusions

The microwave-assisted synthesis process was used to create the flower-like structured MnMoO₄. XRD examination was utilized to confirm the monoclinic phase structure and the crystalline environment of the synthesized MnMoO₄ flowers. Further, the chemical bonding of the molecule and the functional group identification of the MnMoO₄ flowers were characterized via XPS, FTIR, and Raman analyses. The direct bandgap of 2.3 eV of the MnMoO₄ was determined from the UV vis-DRS analysis and the flower-like structured morphology of the MnMoO₄ was observed from the FE-SEM analysis. Finally, the produced material was studied for cycle stability and photocatalytic degradation effectiveness toward the organic pollutant MB dye with an irradiation time of 50 min with 85% of the degradation efficiency. Further, the stability of the synthesized photocatalyst was assessed by executing four consecutive runs of the photocatalyst experiments. Also, to investigate its durability, the FE-SEM and XRD analyses were employed with the post-experimental photocatalyst samples. The post-experimental samples exhibited almost the same morphology and crystal structure, with only a small decline in their peak intensities. Thus, the synthesized MnMoO₄ flower-like structured photocatalysts could be highly suitable as applications in wastewater treatment for a longer duration.

Author Contributions: Conceptualization, M.S. and A.K.; methodology, M.S.; software, A.K., M.T., A.A., S.P., E.J.S.S. and E.M.L.S.; formal analysis, M.S., A.A., M.R. and P.C.R.; investigation, M.S., M.R.V. and A.K.; writing—original draft preparation, M.S., A.A. and M.R.V.; writing—review and editing, M.S., A.A., M.R.V. and A.K., E.M.L.S.; supervision, M.S., A.K., E.M.L.S. and M.R.V. All authors have read and agreed to the published version of the manuscript.

Funding: The authors extend their appreciation to the Deputyship for Research and Innovation, “Ministry of Education” in Saudi Arabia for funding this research (IFKSUOR3-573-2). The authors Arulraj Arunachalam and Mangalaraja Ramalinga Viswanathan duly acknowledge the ANID-FONDECYT project No.: 3200076, the Government of Chile, the Universidad Tecnológica Metropolitana (UTEM) and the Universidad Adolfo Ibáñez (UAI), Santiago, Chile.

Institutional Review Board Statement: Not applicable.

Informed Consent Statement: Not applicable.

Data Availability Statement: The data presented in this study are available on request from the corresponding author depending on restrictions, e.g., privacy or ethical concerns. The data are not publicly available due to confidentiality.

Acknowledgments: The authors extend their appreciation to the Deputyship for Research and Innovation, “Ministry of Education” in Saudi Arabia for funding this research (IFKSUOR3-573-2). The authors Arulraj Arunachalam and Mangalaraja Ramalinga Viswanathan duly acknowledge the ANID-FONDECYT project No.: 3200076, the Government of Chile, the Universidad Tecnológica Metropolitana (UTEM) and the Universidad Adolfo Ibáñez (UAI), Santiago, Chile.

Conflicts of Interest: The authors declare that they have no known competing financial interests or personal relationships that could have appeared to influence the work reported in this paper.

References

1. Farid, A.; Michael, V.; Safwat, G. Melatonin Loaded Poly(lactic-Co-Glycolic Acid) (PLGA) Nanoparticles Reduce Inflammation, Inhibit Apoptosis and Protect Rat’s Liver from the Hazardous Effects of CCL4. *Sci. Rep.* **2023**, *13*, 16424. [CrossRef]
2. Jeyachandran, S.; Srinivasan, R.; Ramesh, T.; Parivallal, A.; Lee, J.; Sathiyamoorthi, E. Recent Development and Application of “Nanozyme” Artificial Enzymes—A Review. *Biomimetics* **2023**, *8*, 446. [CrossRef]
3. Nikitha, M.; Elanchezhian, S.S.; Meenakshi, S. Photodegradation of Rhodamine-B in Aqueous Environment Using Visible-Active gCN@CS-MoS Nanocomposite. *Environ. Res.* **2023**, *238*, 117032. [CrossRef]
4. Kheskwani, U.; Ahammed, M.M. Removal of Water Pollutants Using Plant-Based Nanoscale Zero-Valent Iron: A Review. *Water Sci. Technol.* **2023**, *88*, 1207–1231. [CrossRef]
5. Gayathri, P.V.; Rayaroth, M.P.; Aravindakumar, C.T.; Pillai, D.; Joseph, S. SUNLIGHT-INDUCED Decontamination of Water from Emerging Pharmaceutical Pollutants Using ZnO Nanoparticles. *Chemosphere* **2023**, *343*, 140265. [CrossRef]
6. Fang, J.; Wei, S.; Gao, Y.; Zhang, X.; Cheng, Y.; Wang, J.; Ma, J.; Shi, G.; Bai, L.; Xie, R.; et al. Character Variation of Root Space Microbial Community Composition in the Response of Drought-Tolerant Spring Wheat to Drought Stress. *Front. Microbiol.* **2023**, *14*, 1235708. [CrossRef]
7. Czerwionka, K.; Wilinska, A.; Tuszyńska, A. The Use of Organic Coagulants in the Primary Precipitation Process at Wastewater Treatment Plants. *Water* **2020**, *12*, 1650. [CrossRef]
8. Charles, J.; Bradu, C.; Morin-Crini, N.; Sancey, B.; Winterton, P.; Torri, G.; Badot, P.-M.; Crini, G. Pollutant Removal from Industrial Discharge Water Using Individual and Combined Effects of Adsorption and Ion-Exchange Processes: Chemical Abatement. *J. Saudi Chem. Soc.* **2016**, *20*, 185–194. [CrossRef]
9. Mehdizadeh, P.; Amiri, O.; Rashki, S.; Salavati-Niasari, M.; Salimian, M.; Foong, L.K. Effective Removal of Organic Pollution by Using Sonochemical Prepared LaFeO₃ Perovskite under Visible Light. *Ultrason. Sonochem.* **2020**, *61*, 104848. [CrossRef] [PubMed]
10. Titchou, F.E.; Zazou, H.; Afanga, H.; El Gaayda, J.; Akbour, R.A.; Hamdani, M. Removal of Persistent Organic Pollutants (POPs) from Water and Wastewater by Adsorption and Electrocoagulation Process. *Groundw. Sustain. Dev.* **2021**, *13*, 100575. [CrossRef]
11. Shokri, A.; Fard, M.S. A Critical Review in Fenton-like Approach for the Removal of Pollutants in the Aqueous Environment. *Environ. Chall.* **2022**, *7*, 100534. [CrossRef]
12. Remache, W.; Ramos, D.R.; Mammeri, L.; Boucheloukh, H.; Marín, Z.; Belaidi, S.; Sehili, T.; Santaballa, J.A.; Canle, M. An Efficient Green Photo-Fenton System for the Degradation of Organic Pollutants. Kinetics of Propranolol Removal from Different Water Matrices. *J. Water Proc. Eng.* **2022**, *46*, 102514. [CrossRef]
13. Selvamani, M.; Alsulmi, A.; Sundaramoorthy, A.; Vadivel, S.; Kesavan, A.V. Synthesis of ZnWO₄ Nanorods: The Photocatalytic Effects on RhB Dye Degradation upon Irradiation with Sunlight Light. *J. Mater. Sci. Mater. Electron.* **2023**, *34*, 2094. [CrossRef]
14. Liu, N.; Yu, J.; Zhang, H.; Zhu, J.; Liu, Q.; Chen, R.; Li, Y.; Li, R.; Wang, J. Fe-MMT/WO Composites for Chemical and Photocatalysis Synergistic Reduction of Uranium (VI). *Chemosphere* **2023**, *344*, 140321. [CrossRef]

15. Etemadi, H.; Soltani, T.; Yoshida, H.; Zhang, Y.; Telfer, S.G.; Buchanan, J.K.; Plieger, P.G. Synergistic Effect of Redox Dual PdO/MnO Cocatalysts on the Enhanced H Production Potential of a SnS/ α -FeO Heterojunction via Ethanol Photoreforming. *ACS Omega* **2022**, *7*, 42347–42358. [[CrossRef](#)]
16. Kumar, P.S.; Biju, C.S.; Johnson, J. Influence of Annealing on the Structural, Morphological, Photoluminescence and Visible Absorption Properties of Mg Doped CuO Micro Grains. *J. Fluoresc.* **2023**. [[CrossRef](#)] [[PubMed](#)]
17. Gaffar, S.; Kumar, A.; Alam, J.; Riaz, U. Efficient Visible Light-Induced Photocatalytic Degradation of Tetracycline Hydrochloride Using CuFeO and PANI/CuFeO Nanohybrids. *Environ. Sci. Pollut. Res. Int.* **2023**, *30*, 108878–108888. [[CrossRef](#)] [[PubMed](#)]
18. Tong, Y.; Zhang, Z.; Hou, Y.; Yan, L.; Chen, X.; Zhang, H.; Wang, X.; Li, Y. Recent Progress of Molybdenum Carbide Based Electrocatalysts for Electrocatalytic Hydrogen Evolution Reaction. *Nanoscale* **2023**, *15*, 14717–14736. [[CrossRef](#)] [[PubMed](#)]
19. Xu, C.; Chang, P.; Liu, Z.; Guan, L.; Wang, X.; Tao, J. Electrochemical Activated Molybdenum Oxides Based Multiphase Heterostructures with High Hydrogen Evolution Activity in Alkaline Condition. *Nanotechnology* **2023**, *34*, 465402. [[CrossRef](#)]
20. Mitsumoto, T.; Ashida, Y.; Arashiba, K.; Kuriyama, S.; Egi, A.; Tanaka, H.; Yoshizawa, K.; Nishibayashi, Y. Catalytic Activity of Molybdenum Complexes Bearing PNP-Type Pincer Ligand toward Ammonia Formation. *Angew. Chem. Int. Ed. Engl.* **2023**, *135*, e202306631. [[CrossRef](#)]
21. Muthamizh, S.; Sengottaiyan, C.; Jayavel, R.; Narayanan, V. Facile Synthesis of Phase Tunable MoO₃ Nanostructures and Their Electrochemical Sensing Properties. *J. Nanosci. Nanotechnol.* **2020**, *20*, 2823–2831. [[CrossRef](#)] [[PubMed](#)]
22. Qin, L.; Huang, S.; Cheng, H. Catalytic Performance and Mechanism of Bismuth Molybdate Nanosheets Decorated with Platinum Nanoparticles for Formaldehyde Decomposition at Room Temperature. *J. Colloid Interface Sci.* **2023**, *633*, 453–467. [[CrossRef](#)] [[PubMed](#)]
23. Wu, T.H.; Liu, Y.S.; Hong, C.T.; Hou, B.-W. Binary and Nanostructured NiMn Perovskite Fluorides as Efficient Electrocatalysts for Urea Oxidation Reaction. *J. Colloid Interface Sci.* **2023**, *653*, 1094–1102. [[CrossRef](#)] [[PubMed](#)]
24. Abbas, Q.; Khurshid, H.; Yoosuf, R.; Lawrence, J.; Issa, B.A.; Abdelkareem, M.A.; Olabi, A.G. Engineering of Nickel, Cobalt Oxides and Nickel/cobalt Binary Oxides by Electrodeposition and Application as Binder Free Electrodes in Supercapacitors. *Sci. Rep.* **2023**, *13*, 15654. [[CrossRef](#)] [[PubMed](#)]
25. Wu, Q.; Chen, L.; Kuo, D.-H.; Li, P.; Abdeta, A.B.; Zelekew, O.A.; Lin, J.; Chen, X. Sulfur Substitution and Defect Engineering in an Unfavored MnMoO Catalyst for Efficient Hydrogen Evolution under Visible Light. *ACS Appl. Mater. Interfaces* **2023**, *15*, 22142–22156. [[CrossRef](#)]
26. Tamboli, M.S.; Patil, S.A.; Tamboli, A.M.; Patil, S.S.; Truong, N.T.N.; Lee, K.; Praveen, C.S.; Shrestha, N.K.; Park, C.; Kale, B.B. Polyaniline-Wrapped MnMoO as an Active Catalyst for Hydrogen Production by Electrochemical Water Splitting. *Dalton Trans.* **2022**, *51*, 6027–6035. [[CrossRef](#)]
27. Jabeen, S.; Kumar, P.; Samra, K.S. Boosting the Electrochemical Characteristics of MnMoO₄ Nanoparticles for Supercapacitor Applications. *J. Appl. Electrochem.* **2023**. [[CrossRef](#)]
28. Venkatesh, K.; Rajakumaran, R.; Chen, S.-M.; Karuppiah, C.; Yang, C.-C.; Ramaraj, S.K.; Ali, M.A.; Al-Hemaid, F.M.A.; El-Shikh, M.S.; Almunqedhi, B.M.A. A Novel Hybrid Construction of MnMoO Nanorods Anchored Graphene Nanosheets; an Efficient Electrocatalyst for the Picomolar Detection of Ecological Pollutant Ornidazole in Water and Urine Samples. *Chemosphere* **2021**, *273*, 129665. [[CrossRef](#)]
29. Muthamizh, S.; Suresh, R.; Giribabu, K.; Manigandan, R.; Praveen Kumar, S.; Munusamy, S.; Narayanan, V. MnWO₄ Nanocapsules: Synthesis, Characterization and Its Electrochemical Sensing Property. *J. Alloys Compd.* **2015**, *619*, 601–609. [[CrossRef](#)]
30. Ranjith, K.S.; Ezhil Vilian, A.T.; Ghoreishian, S.M.; Umapathi, R.; Hwang, S.-K.; Oh, C.W.; Huh, Y.S.; Han, Y.-K. Hybridized 1D-2D MnMoO-MXene Nanocomposites as High-Performing Electrochemical Sensing Platform for the Sensitive Detection of Dihydroxybenzene Isomers in Wastewater Samples. *J. Hazards Mater.* **2022**, *421*, 126775. [[CrossRef](#)] [[PubMed](#)]
31. Wang, X.; Gao, Z.; Wang, C.; Guo, X.; Sun, Y.; Jia, Y.; Tao, X. Design, Growth, and Characterization of YMoO Crystals for Raman Laser Applications. *RSC Adv.* **2020**, *11*, 1164–1171. [[CrossRef](#)]
32. Wu, Q.; Gao, Z.; Wu, Z.; Li, C.; Tian, X.; Zhao, P.; Wang, Z.; Sun, Y.; Xia, S.; Tao, X. Generation of a Simultaneous Orthogonally Polarized Dual-Wavelength Raman Laser with Power Ratio Tunability by a Single Hexagonal Crystal: CsTeMoO. *Opt. Lett.* **2020**, *45*, 5061–5064. [[CrossRef](#)]
33. Ajam, M.; Ehteshami, M.; Boudaghpour, S.; Mirbagheri, S.A.; Kafil, M. Tetracycline Removal from Aqueous Solution by Biochar Derived from Algae and Modified with MnMoO: Effects of Operating Parameters, Isotherm, Kinetic, and Thermodynamic Study. *Int. J. Phytoremediat.* **2022**, *24*, 975–986. [[CrossRef](#)]
34. da Silveira Lacerda, L.H.; San-Miguel, M.A. Unraveling the MnMoO₄ Polymorphism: A Comprehensive DFT Investigation of α , β , and ω Phases. *J. Mater. Sci.* **2022**, *57*, 10179–10196. [[CrossRef](#)] [[PubMed](#)]
35. Ghosh, D.; Giri, S.; Moniruzzaman, M.; Basu, T.; Mandal, M.; Das, C.K. α MnMoO₄/graphene Hybrid Composite: High Energy Density Supercapacitor Electrode Material. *Dalton Trans.* **2014**, *43*, 11067–11076. [[CrossRef](#)]
36. Chandhana, J.P.; Punnakkal, N.; Vasu, S.P.; Pradeep, A.; Nair, B.G.; Babu, T.G.S. Zirconium Copper Oxide Microflowers Based Non-Enzymatic Screen-Printed Electrochemical Sensor for the Detection of Glucose in Saliva, Urine, and Blood Serum. *Mikrochim. Acta* **2023**, *190*, 390.
37. Orudzhev, F.; Sobola, D.; Ramazanov, S.; Částková, K.; Papež, N.; Selimov, D.A.; Abdurakhmanov, M.; Shuaibov, A.; Rabadanova, A.; Gulakhmedov, R.; et al. Piezo-Enhanced Photocatalytic Activity of the Electrospun Fibrous Magnetic PVDF/BiFeO₃ Membrane. *Polymers* **2023**, *15*, 246. [[CrossRef](#)]

38. Garg, A.; Chauhan, A.; Agnihotri, C.; Singh, B.P.; Mondem, V.; Basu, S.; Agnihotri, S. Sunlight Active Cellulose/g-CN/TiO₂ Nano-Photocatalyst for Simultaneous Degradation of Methylene Blue Dye and Atenolol Drug in Real Wastewater. *Nanotechnology* **2023**, *34*, 505705. [[CrossRef](#)]
39. Abdrabou, D.; Ahmed, M.; Hussein, A.; El-Sherbini, T. Photocatalytic Behavior for Removal of Methylene Blue from Aqueous Solutions via Nanocomposites Based on GdO/CdS and Cellulose Acetate Nanofibers. *Environ. Sci. Pollut. Res. Int.* **2023**, *30*, 99789–99808. [[CrossRef](#)] [[PubMed](#)]
40. Dao, T.D.; Han, G.; Arai, N.; Nabatame, T.; Wada, Y.; Hoang, C.V.; Aono, M.; Nagao, T. Plasmon-Mediated Photocatalytic Activity of Wet-Chemically Prepared ZnO Nanowire Arrays. *Phys. Chem. Chem. Phys.* **2015**, *17*, 7395–7403. [[CrossRef](#)]
41. Ngullie, R.C.; Alaswad, S.O.; Bhuvaneswari, K.; Shanmugam, P.; Pazhanivel, T.; Arunachalam, P. Synthesis and Characterization of Efficient ZnO/g-C₃N₄ Nanocomposites Photocatalyst for Photocatalytic Degradation of Methylene Blue. *Coatings* **2020**, *10*, 500. [[CrossRef](#)]
42. Ren, B.; Miao, J.; Xu, Y.; Zhai, Z.; Dong, X.; Wang, S.; Zhang, L.; Liu, Z. A Grape-like N-Doped Carbon/CuO-Fe₂O₃ Nanocomposite as a Highly Active Heterogeneous Fenton-like Catalyst in Methylene Blue Degradation. *J. Clean. Prod.* **2019**, *240*, 118143. [[CrossRef](#)]
43. Prabakaran, E.; Pillay, K. Synthesis of N-Doped ZnO Nanoparticles with Cabbage Morphology as a Catalyst for the Efficient Photocatalytic Degradation of Methylene Blue under UV and Visible Light. *RSC Adv.* **2019**, *9*, 7509–7535. [[CrossRef](#)] [[PubMed](#)]
44. Kirankumar, V.S.; Mayank, N.; Sumathi, S. Photocatalytic Performance of Cerium Doped Copper Aluminate Nanoparticles under Visible Light Irradiation. *J. Taiwan Inst. Chem. Eng.* **2019**, *95*, 602–615. [[CrossRef](#)]
45. Min, S.; Wang, F.; Jin, Z.; Xu, J. Cu₂O Nanoparticles Decorated BiVO₄ as an Effective Visible-Light-Driven p-n Heterojunction Photocatalyst for Methylene Blue Degradation. *Superlattices Microstruct.* **2014**, *74*, 294–307. [[CrossRef](#)]

Disclaimer/Publisher's Note: The statements, opinions and data contained in all publications are solely those of the individual author(s) and contributor(s) and not of MDPI and/or the editor(s). MDPI and/or the editor(s) disclaim responsibility for any injury to people or property resulting from any ideas, methods, instructions or products referred to in the content.